SUBMITTED TO APJ LETTERS ON 2013 SEPTEMBER 10
Preprint typeset using LaTeX style emulateapj v. 04/17/13

REVIVAL OF THE STALLED CORE-COLLAPSE SUPERNOVA SHOCK TRIGGERED BY PRECOLLAPSE ASPHERICITY IN THE PROGENITOR STAR

SEAN M. COUCH[1,*] AND CHRISTIAN D. OTT[2,3,+]

Submitted to ApJ Letters on 2013 September 10

ABSTRACT

Multi-dimensional simulations of advanced nuclear burning stages of massive stars suggest that the Si/O layers of presupernova stars harbor large deviations from the spherical symmetry typically assumed for presupernova stellar structure. We carry out three-dimensional core-collapse supernova simulations with and without aspherical velocity perturbations to assess their potential impact on the supernova hydrodynamics in the stalled shock phase. Our results show that realistic perturbations can qualitatively alter the postbounce evolution, triggering an explosion in a model that fails to explode without them. This finding underlines the need for a multi-dimensional treatment of the presupernova stage of stellar evolution.

Keywords: hydrodynamics – neutrinos – Stars: supernovae: general

1. INTRODUCTION

The core-collapse supernova (CCSN) phenomenon is fundamentally multi-dimensional. Axisymmetric (2D) and three-dimensional (3D) simulations have shown that convection and the standing accretion shock instability (SASI) robustly break spherical symmetry in the pre-explosion stalled-shock phase (see, e.g., Couch & O'Connor 2013; Couch 2013; Ott et al. 2013; Dolence et al. 2013; Hanke et al. 2013; Takiwaki et al. 2013 for recent 3D simulations). The propagation of artificially initiated explosions through the progenitor envelope found that symmetry is broken by Rayleigh-Taylor and Richtmyer-Meshkov instabilities (e.g., Couch et al. 2009; Hammer et al. 2010; Joggerst et al. 2010). The conclusions of these simulations are backed up by observations of asphericities in local supernova remnants (Vink 2012), by spectropolarimetry of distant CCSNe (Wang & Wheeler 2008; Chornock et al. 2011, and references therein), and by pulsar kicks (e.g., Hobbs et al. 2005).

For initial conditions based on 1D stellar evolutionary models, the breaking of spherical symmetry after the initial collapse and bounce of the inner core is widely appreciated. Stars, however, are not truly spherical. Yet, the current state-of-the-art in CCSN progenitor evolution is 1D. Such models resort to various kludges to account for multi-D phenomena such as convection, rotation, and magnetic fields (see Langer 2012 for a review). Exploratory explicit multi-D hydrodynamics simulations of the Si/O-shell burning stage prior to core collapse (Bazan & Arnett 1998; Meakin & Arnett 2007; Arnett & Meakin 2011) have shown that violent fluctuations about the mean turbulent flow can lead to low-mode deviations from spherical symmetry. These fluctuations may also trigger eruptions that partially unbind the stellar envelope, leading to precursor transients weeks to months prior to core collapse (Smith & Arnett 2013, but also see Quataert & Shiode 2012). This has now been observed for multiple CCSNe. The fluctuations and their consequences cannot be captured by the standard mixing-length approach for convection and time-implicit stellar evolution codes (Smith & Arnett 2013).

The perturbations caused by Si/O shell burning fluctuations are part of the supersonically collapsing outer core and may be amplified during collapse (Lai & Goldreich 2000). They reach the stalled shock $\sim 100 - 300\,\mathrm{ms}$ after bounce, depending on the structure of the progenitor. At this time, neutrino-driven convection and/or SASI are active and may be affected by spatial variations in the accretion flow. Burrows & Hayes (1996) were the first to carry out 2D collapse simulations of a progenitor whose density outside $0.9 M_\odot$ was decreased by 15% within a 20° wedge of the pole. They found an early explosion in the direction of the perturbation and a hydrodynamically kicked protoneutron star. Fryer (2004), studied similarly large $\ell = 1$ perturbations applied globally, or only in the Si/O layers, using 3D smooth particle hydrodynamics. He also found neutron star kicks and explosion asymmetries, though of smaller magnitude than observed in 2D.

In this Letter, we examine the role of perturbations on the explosion mechanism *itself*. We carry out 3D simulations of the postbounce evolution of a nonrotating 15-$M_\odot$ progenitor star. Unlike previous work, we apply momentum-preserving tangential velocity perturbations with spatial frequency and magnitude motivated by Bazan & Arnett (1998) and Arnett & Meakin (2011). We also carry out unperturbed control simulations for comparison. Our results demonstrate that asphericities in the Si/O layer increase the strength of turbulence behind the stalled but dynamic shock. This creates conditions more favorable for shock expansion. We show that the perturbations can trigger explosion in a model that would not explode otherwise.

2. METHODS AND SETUP

We simulate 3D Newtonian CCSN postbounce evolution using the FLASH simulation framework (Fryxell et al. 2000; Dubey et al. 2009; Lee et al. 2013).[6] Our basic numerical approach is described by Couch & O'Connor (2013) and Couch (2013). We use the multispecies neutrino leakage scheme of O'Connor & Ott (2010), whose 3D version was also employed in Ott et al. (2012); Ott et al. (2013). The neutrino

[1] Flash Center for Computational Science, Department of Astronomy & Astrophysics, University of Chicago, Chicago, IL, 60637, smc@flash.uchichago.edu
[2] TAPIR, Mailcode 350-17, California Institute of Technology, Pasadena, CA 91125, USA, cott@tapir.caltech.edu
[3] Kavli Institute for the Physics and Mathematics of the Universe (Kavli IPMU WPI), The University of Tokyo, Kashiwa, Japan
[*] Hubble Fellow
[+] Alfred P. Sloan Research Fellow

[6] Available at http://flash.uchicago.edu.

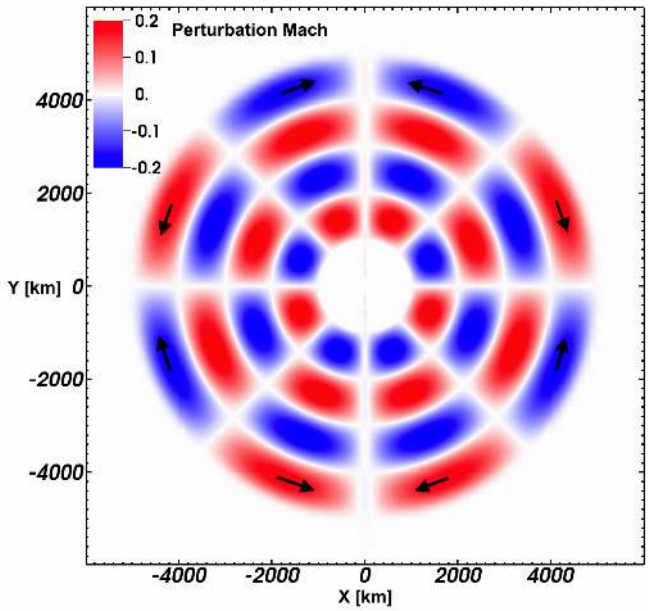

Figure 1. Example of the initial θ-velocity perturbations applied in this study. Shown is the a meridional slice of the Mach number of the θ-direction velocity. The arrows in the outer ring of perturbations show the local velocity directions.

leakage scheme includes a multiplicative factor, $f_{\rm heat}$, in the neutrino heating source term, which can be adjusted to yield more efficient neutrino heating (i.e., $f_{\rm heat} > 1$). The leakage scheme with $f_{\rm heat}$= 1.00 is tuned to match the multiangle, multigroup full neutrino transport simulations of Ott et al. (2008). In all simulations reported here, we use 3D Cartesian geometry with a finest grid spacing $dx_{\rm min} = 0.49$ km. Using adaptive mesh refinement, we achieve a pseudo-logarithmic grid by decrementing the maximum allowed refinement level as a function of radius. The typical effective "angular" resolution is 0.37°.

We use a single progenitor model, the 15-$M_\odot$ star of Woosley & Heger (2007). In order to study the dependence of 3D CCSN simulations on asphericities extant in the progenitor, we apply perturbations to the 1D stellar profile. We seed perturbations that are convolutions of sinusoidal functions of radius and angle. For simplicity, we perturb *only* the velocity in the spherical θ-direction and leave all other variables untouched. The form of the sinusoidal perturbation to v_θ is

$$\delta v_\theta = M_{\rm pert} c_S \sin[(n-1)\theta] \sin[(n-1)\zeta] \cos(n\phi)\,, \quad (1)$$

where $M_{\rm pert}$ is the peak Mach number of the perturbations, c_S is the local adiabatic sound speed, n is the number of nodes in the interval $\theta = [0, \pi]$, and $\zeta = \pi(r - r_{\rm pert,min})/(r_{\rm pert,max} - r_{\rm pert,min})$. The perturbations are only applied within a spherical shell with radial limits $r_{\rm pert,min} < r < r_{\rm pert,max}$. We scale the perturbations with local sound speed so that the peak amplitudes of the perturbations are constant in *Mach* number, not absolute velocity. This results in higher-speed perturbations at smaller radii where the sound speeds are larger. Importantly, for odd node numbers, Eq. (1) results in *zero* net momentum contribution to the inital conditions. We have verified this experimentally to machine-precision.

3. RESULTS

We start our 3D simulations from the results of 1D simulations at 2 ms after core bounce, and it is at this point that we apply the perturbations given by Eq. (1). In the results we discuss here, we use a node count $n = 5$ and peak perturbation Mach number $M_{\rm pert} = 0.2$. This establishes large-scale perturbations that are similar in extent and speed to some convective plumes found in multi-D progenitor burning simulations (Meakin & Arnett 2007; Arnett & Meakin 2011). We choose $r_{\rm pert,min}$ to correspond to the inner edge of the silicon shell (i.e., the outer edge of the iron core). For this progenitor at the time of core bounce, this corresponds to a radius of $\sim$ 1000 km. We set $r_{\rm pert,max} = 5000$ km, which is sufficiently large to never reach the shock during the simulated time period. Figure 1 shows a pseudo-color plot of the perturbations used in this study.

We present the results of four 3D simulations, two perturbed and two unperturbed. We use two different heat factors for both perturbed and unperturbed case: $f_{\rm heat}$= 1.00 and a slightly enhanced heating case with $f_{\rm heat}$= 1.02. We refer to the simulations using the scheme n[*node count*]m[*initial perturbation Mach number, times ten*] $f_{\rm heat}$[*heat factor*], such that the perturbed model with enhanced heat factor is referred to as 'n5m2 $f_{\rm heat}$1.02.'

We find that introducing plausibly-scaled velocity perturbations in the Si shell of the progenitor star can trigger a successful explosion for cases in which an unperturbed simulation fails. Figure 2 shows several entropy volume renderings for models n0m0 $f_{\rm heat}$1.02 and n5m2 $f_{\rm heat}$1.02 at three postbounce times. The only difference between these two models is the presence of initial velocity perturbations in the Si/O layer. Model n5m2 $f_{\rm heat}$1.02 results in continued runaway shock expansion and asymmetric explosion, as clearly shown, while model n0m0 $f_{\rm heat}$1.02 fails to explode and the shock recedes to small radii. At 100 ms, only shortly after the perturbations have reached the shock, both simulations are quite similar showing strong convection following the preceding period of shock expansion. By 200 ms, however, differences in the models are obvious. The shock has already begun to recede in n0m0 $f_{\rm heat}$1.02 while model n5m2 $f_{\rm heat}$1.02 has retained a large shock radius and is on the verge of runaway shock expansion. The last frames show the final states of the two simulations. Model n5m2 $f_{\rm heat}$1.02 has exploded, resulting in a large, asymmetric shock structure, while the shock has fallen back to $\sim$100 km in model n0m0 $f_{\rm heat}$1.02.

In Figure 3, we present the time evolutions of several global metrics for our four 3D simulations. The top panel of Fig. 3 shows the average shock radius. All models, with the exception of n5m2 $f_{\rm heat}$1.02, fail to explode. Compared with the control case, n0m0 $f_{\rm heat}$1.00, both n0m0 $f_{\rm heat}$1.02 and n5m2 $f_{\rm heat}$1.00 show longer stalled-shock phases prior to shock recession. These two intermediate cases, despite employing different heat factors, show remarkably similar average shock radius histories. In the case of the successful explosion, n5m2 $f_{\rm heat}$1.02, the average shock radius remains extremely similar to the comparable unperturbed model, n0m0 $f_{\rm heat}$1.02, until about 100 ms after bounce. The average shock radius of n5m2 $f_{\rm heat}$1.02 remains relatively constant just below 200 km until $t_{\rm pb} \sim 200$ ms at which point the shock begins to expand rapidly, signaling the onset of explosion.

The second panel of Fig. 3 shows a measure of the overall shock asymmetry, the normalized standard deviation of the shock radius $\tilde{\sigma}$. The shock asymmetry grows as n5m2 $f_{\rm heat}$1.02 experiences runaway shock expansion, indicating that the explosion is aspherical, as is also clear from the bottom-right panel of Fig. 2. The failed explosions show comparatively small values of $\tilde{\sigma}$, implying relative sphericity of

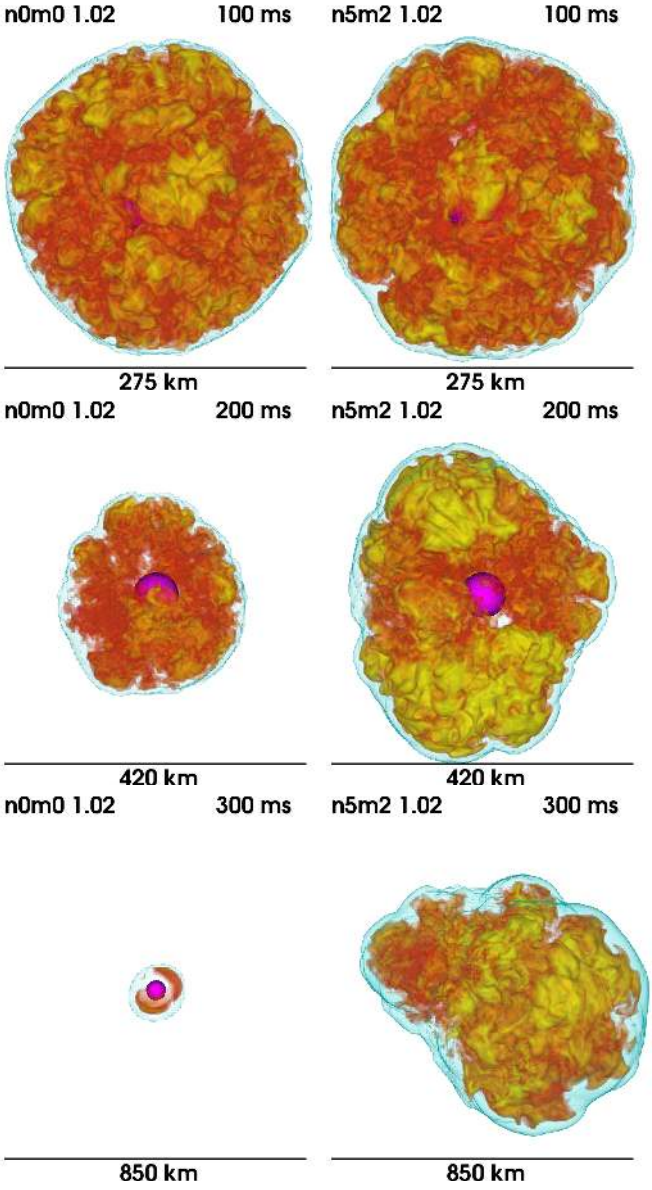

Figure 2. Volume renderings of entropy for models n0m0 $f_{\rm heat}1.02$ (left column) and n5m2 $f_{\rm heat}1.02$ (right column) at three different postbounce times, from top to bottom: 100 ms, 200 ms, and 300 ms. The spatial scale is noted at the bottom of each pane and increases with time. The PNS is visible in the center of the renderings, marked by a magenta constant-density contour with value 10^{12} g cm^{-3}.

the shock surface, until strong SASI oscillations set in after the shock has receded (see Couch & O'Connor 2013).

The presence of pre-shock perturbations has substantial impact on the neutrino heating efficiency, $\eta = Q_{\rm net}(L_{\nu_e} + L_{\bar{\nu}_e})^{-1}$. As shown in the third panel of Fig. 3, for n5m2 $f_{\rm heat}1.00$, the heating efficiency history is very similar to that of n0m0 $f_{\rm heat}1.02$. This implies that the perturbations drive nonradial motion that increases the dwell time of material in the gain region, significantly enhancing the fraction of neutrino luminosity absorbed. For n5m2 $f_{\rm heat}1.02$, the combination of $f_{\rm heat} > 1$ *and* pre-shock perturbations results in a sufficiently increased heating efficiency to initiate a neutrino-driven explosion. Also, η depends sensitively, and nonlinearly, on $f_{\rm heat}$. The time-averaged heating efficiencies for simulations n0m0 $f_{\rm heat}1.00$, n0m0 $f_{\rm heat}1.02$, n5m2 $f_{\rm heat}1.00$, and n5m2 $f_{\rm heat}1.02$ are 0.062, 0.080, 0.075, and 0.100, respectively.

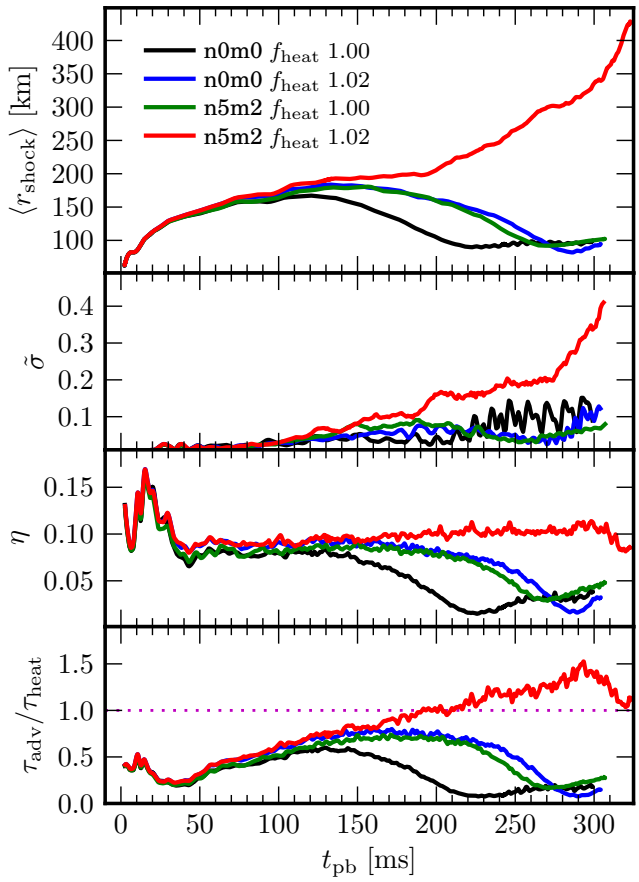

Figure 3. Time evolution of the global explosion diagnostics for our simulations. Four 3D simulations are shown: unperturbed models with $f_{\rm heat}1.00$ (black lines) and 1.02 (blue lines), and perturbed models with $f_{\rm heat}1.00$ (green lines) and 1.02 (red lines). The top panel shows the average shock radius. The second panel shows the normalized standard deviation of the shock radius, $\tilde{\sigma} = \langle r_{\rm shock}\rangle^{-1}[(4\pi)^{-1}\int d\Omega(r_{\rm shock} - \langle r_{\rm shock}\rangle)^2]^{1/2}$. The third panel shows the heating efficiency, $\eta = Q_{\rm net}(L_{\nu_e} + L_{\bar{\nu}_e})^{-1}$. The bottom panel shows the ratio of advection-to-heating time scales.

It is almost exactly at the positive inflection in the average shock radius curve of n5m2 $f_{\rm heat}1.02$ ($\sim$ 200 ms) that the critical condition for explosion, $\tau_{\rm adv}/\tau_{\rm heat} > 1$ is satisfied (Fig. 3; Thompson 2000; Janka 2001; Buras et al. 2006; Fernández 2012). Here we define the average advection time through the gain region as $\tau_{\rm adv} = M_{\rm gain}/\dot{M}$ and the gain region heating time as $\tau_{\rm heat} = |E_{\rm gain}|/Q_{\rm net}$, where $|E_{\rm gain}|$ is the total specific energy of the gain region and $Q_{\rm net}$ is the net neutrino heating in the gain region (c.f. Müller et al. 2012; Ott et al. 2013). During the stalled-shock phase of n5m2 $f_{\rm heat}1.02$, around $100 - 200$ ms, the ratio $\tau_{\rm adv}/\tau_{\rm heat}$ is growing continuously. Once this critical ratio exceeds unity, thermal energy builds up in the gain region faster than it can be advected out into the cooling layer and the shock begins to expand.

In order to assess the magnitude of the perturbations as they are actually impinging upon the shock, and their effect on the turbulent postbounce flow, we compute the density-weighted radial averages of the Mach number of anisotropic motion,

$$\langle M_{\rm aniso}\rangle = \left\langle \frac{v_{\rm aniso}}{\langle c_S\rangle_{4\pi}} \right\rangle_r , \qquad (2)$$

where the sound speed is first angle-averaged and the velocity

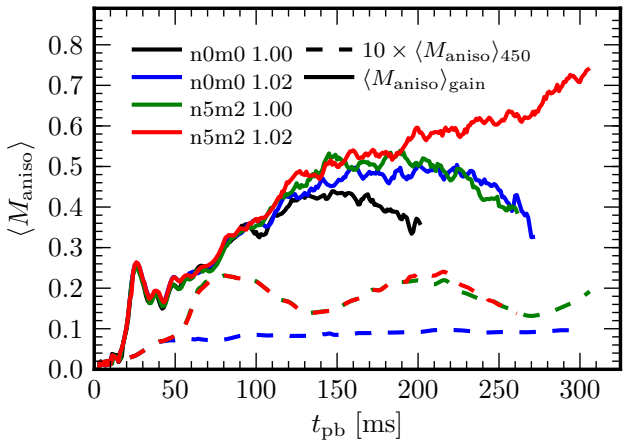

Figure 4. Density-weighted average of the Mach number of anisotropic motion [Eq. (2)] in two separate regions: the gain region (solid lines) and a 100-km wide spherical shell centered on $r = 450$ km (dashed lines, multiplied by 10).

of anisotropic motion has the same definition as in Ott et al. (2013); Couch & O'Connor (2013). The anisotropic Mach numbers for the gain layer and for the preshock radial interval $400 - 500$ km are shown in Fig. 4. The differences between $\langle M_{\rm aniso}\rangle_{450}$ for perturbed and unperturbed cases are evident. The unperturbed cases, n0m0 $f_{\rm heat}1.00$ and n0m0 $f_{\rm heat}1.02$, have $\langle M_{\rm aniso}\rangle_{450} \lesssim 0.01$, whereas in the perturbed models we find peak values of $\langle M_{\rm aniso}\rangle_{450}$ of $\gtrsim$0.02. The Mach number of the perturbations is dramatically reduced by the compression resulting from infall toward the shock. Larger preshock values of $\langle M_{\rm aniso}\rangle$ correlate with larger post-shock values of $\langle M_{\rm aniso}\rangle$. The perturbed models for both low and high heat factors show similarly large values of $\langle M_{\rm aniso}\rangle_{\rm gain}$ until ~ 200 ms when n5m2 $f_{\rm heat}1.02$ begins to explode. The unperturbed models have lower values of $\langle M_{\rm aniso}\rangle_{\rm gain}$ than either perturbed model. The Mach number of anisotropic motion for n0m0 $f_{\rm heat}1.02$ overtakes that of n5m2 $f_{\rm heat}1.00$ around 220 ms, which we attribute to stronger neutrino-driven convection.

Another useful metric of the character of the disturbances reaching the shock is the power spectrum of the perturbations, which we show in Fig. 5. We define the power spectrum of the perturbations to a scalar field X as $\delta_\ell^X = P_\ell^{X,\rm perturbed} - P_\ell^{X,\rm unperturbed}$, where

$$P_\ell^X = \sum_{m=-\ell}^{\ell} \left[\oint X(\theta,\phi) Y_\ell^m(\theta,\phi) d\Omega \right]^2 . \qquad (3)$$

The spherical harmonics, Y_ℓ^m, have their usual definition, and details of similar calculations may be found in, e.g., Hanke et al. (2012); Dolence et al. (2013); Couch (2013). Figure 5 shows the perturbations for tangential velocity, $v_{\rm tan} = \sqrt{v_\theta^2 + v_\phi^2}$, and density, where we have set X to the square root of these quantities so δ_ℓ^X has units of velocity and density, respectively. We normalize $\delta_\ell^{v_{\rm tan},\rho}$ by the angle-averaged radial velocity and density at 400 km, respectively. The applied perturbations to v_θ manifest themselves in peak values of $\delta_\ell^{v_{\rm tan},\rho}$ of $\sim 6\%$ at $\ell = 8$. Nonradial motion caused by the initial perturbations results in the growth of density contrasts during infall (Lai & Goldreich 2000). The peak values of δ_ℓ^ρ correspond to density contrasts reaching the shock front

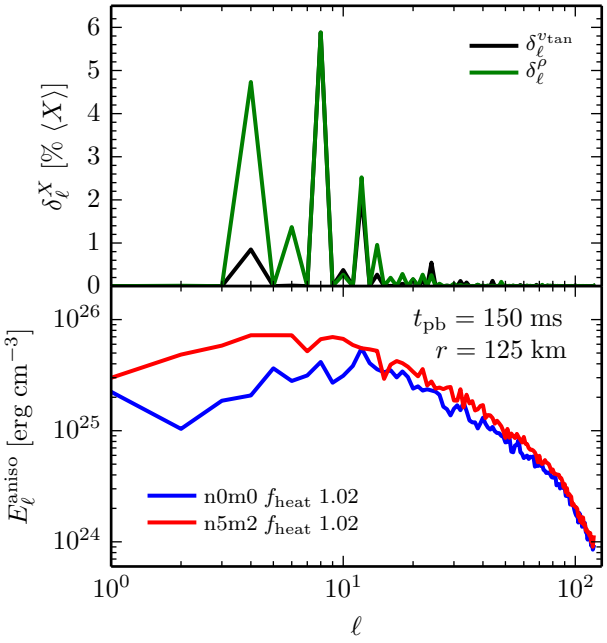

Figure 5. Power spectra in spherical harmonic basis of the perturbations in the pre-shock accretion flow (top). The perturbation spectra are computed as the difference of the sums of the squared spherical harmonic coefficients between the perturbed and unperturbed models, n5m2 $f_{\rm heat}1.02$ and n0m0 $f_{\rm heat}1.00$ [Eq. (3)]. The spectra are computed within a 10 km-wide shell centered on $r = 400$ km and averaged over the 10 ms around $t_{\rm pb} = 100$ ms. Shown are the normalized perturbation spectra of the tangetial velocity (black lines), and of the density field (green lines). We normalize $\delta_\ell^{v_{\rm tan}}$ by the spherically-averaged *radial* velocity at $r = 400$ km. The bottom panel shows the anisotropic kinetic energy spectra in the gain region at $t_{\rm pb} = 150$ ms. The spectra are averaged over a 10 km-wide shell centered on $r = 125$ km and averaged over 10 ms. The anisotropic kinetic energy spectra give a measure of the effect of the perturbations on the nonradial flow in the gain region.

of $\gtrsim 2 \times 10^6$ g cm^{-3}.

Also shown in Fig. 5 is a powerful diagnostic of the strength of convective and turbulent motions in the gain region, the spectrum of anisotropic kinetic energy, $E_\ell^{\rm aniso}$. It is computed from Eq. (3) with $X = \sqrt{\rho[(v_r - \langle v_r\rangle_{4\pi})^2 + v_\theta^2 + v_\phi^2]}$. Model n5m2 $f_{\rm heat}1.02$ has *significantly* more anisotropic kinetic energy at large scales than the unperturbed simulation, n0m0 $f_{\rm heat}1.02$. Above $\ell \approx 10$, the spectra of the perturbed and unperturbed cases become fairly similar. The more dramatic difference at small $\ell's$ corresponds to the spatial scales of the perturbations that are reaching the shock, as measured by δ_ℓ. Kinetic energy on large scales has been noted to correlate with conditions favorable for explosion in a number of previous studies (e.g., Hanke et al. 2012; Couch 2013).

In summary, the message of the various analyses we present in Figs. 3–5 is clear: models with perturbations develop more vigorous postbounce turbulence, have higher neutrino heating efficiencies, and either explode or are much closer to explosion than their unperturbed counterparts. It is particularly noteworthy that the perturbations boost model n5m2 $f_{\rm heat}1.00$ to essentially the same heating efficiency and shock radius evolution as the unperturbed, more strongly heated model n0m0 $f_{\rm heat}1.02$. As pointed out by Foglizzo et al. (2006) and first demonstrated by Scheck et al. (2008), the development and strength of neutrino-driven convection in the gain layer increases with increasing magnitude of the accreting seed perturbations. Stronger nonradial motion increases the

dwell time of material in the gain layer. Thus, our models with perturbations absorb neutrino energy more efficiently, which favors explosion (c.f. Thompson et al. 2005; Murphy & Burrows 2008).

4. CONCLUSIONS

The final phase of nuclear burning in massive stars approaching core collapse is fast and furious. The Si/O shells surrounding the iron core are sites of large-scale deviations of turbulent flow from spherical symmetry. Our 3D postbounce CCSN simulations show that aspherical perturbations in the Si/O layer can have important effects on the 3D hydrodynamics of CCSNe. They lead to more vigorous turbulent flow behind the shock and *qualitatively* alter the outcome of core collapse: they can turn a dud into an explosion.

The nonradial momentum-preserving velocity perturbations that we considered here have spatial frequency and Mach numbers comparable to what is expected from 2D Si/O burning simulations (Bazan & Arnett 1998; Arnett & Meakin 2011). These perturbations are mild compared to the large $\ell = 1$ density variations imposed by the previous studies of Burrows & Hayes (1996) and Fryer (2004).

Our simulations *prove the principle* that nonradial velocity perturbations from convective Si/O burning can alter postbounce CCSN hydrodynamics and can affect the explosion mechanism. We study the effect of only one particular perturbation, however, it is likely that the outcome will depend on both magnitude and spatial dependence of the perturbations. This must be explored in future work. The 3D oxygen burning simulations of Meakin & Arnett (2007) suggest that in 3D the Mach numbers of fluctuations may be only half as large as in 2D. However, Meakin & Arnett (2007) included only the O shell in 3D and Arnett & Meakin (2011) argue that it is the interplay of Si and O burning shells that drives the most violent fluctuations. Thus, we feel that our Mach 0.2 perturbations in the Si/O layer in 3D are *plausible*.

Recent studies comparing 2D and 3D CCSN hydrodynamics suggest that explosions are more readily obtained in 2D than in 3D (Hanke et al. 2012; Couch & O'Connor 2013; Couch 2013; Hanke et al. 2013; Takiwaki et al. 2013, but see Dolence et al. 2013 for a differing view). CCSN theory, however, must robustly produce and explain explosions in 3D to match observations. There are efforts underway by many groups to improve upon current 3D simulations in treatments of neutrino transport, weak interaction physics, magnetic fields, and gravity with the hope of robustly producing explosions in 3D. Our work shows that the initial conditions also matter, reminding us that the CCSN mechanism is essentially an initial value problem. At least part of the solution to the long-standing supernova problem must lie in multi-D progenitor structure. Full-core, full-3D progenitor evolution simulations to the onset of iron core collapse are urgently needed.

ACKNOWLEDGEMENTS

We acknowledge helpful discussions with E. Abdikamalov, D. Arnett, P. Goldreich, C. Graziani, C. Meakin, E. O'Connor, U. C. T. Gamma, C. Reisswig, L. Roberts, and N. Smith. SMC is supported by NASA through Hubble Fellowship grant No. 51286.01 awarded by the Space Telescope Science Institute. CDO is partially supported by NSF grant nos. AST-1212170, PHY-1151197, and OCI-0905046 and by the Alfred P. Sloan Foundation.

The software used in this work was in part developed by the DOE NNSA-ASC OASCR Flash Center at the University of Chicago. The simulations were carried out on computational resources at ALCF at ANL, which is supported by the Office of Science of the US Department of Energy under Contract No. DE-AC02-06CH11357, and on the NSF XSEDE network under computer time allocation TG-PHY100033.

REFERENCES

Arnett, W. D., & Meakin, C. 2011, ApJ, 733, 78
Bazan, G., & Arnett, D. 1998, ApJ, 496, 316
Buras, R., Janka, H.-T., Rampp, M., & Kifonidis, K. 2006, A&A, 457, 281
Burrows, A., & Hayes, J. 1996, Phys. Rev. Lett., 76, 352
Chornock, R., Filippenko, A. V., Li, W., et al. 2011, ApJ, 739, 41
Couch, S. M. 2013, ApJ, 775, 35
Couch, S. M., & O'Connor, E. P. 2013, in preparation
Couch, S. M., Wheeler, J. C., & Milosavljević, M. 2009, ApJ, 696, 953
Dolence, J. C., Burrows, A., Murphy, J. W., & Nordhaus, J. 2013, ApJ, 765, 110
Dubey, A., Antypas, K., Ganapathy, M. K., et al. 2009, Parallel Computing, 35, 512
Fernández, R. 2012, ApJ, 749, 142
Foglizzo, T., Scheck, L., & Janka, H.-T. 2006, ApJ, 652, 1436
Fryer, C. L. 2004, ApJ, 601, L175
Fryxell, B., Olson, K., Ricker, P., et al. 2000, ApJS, 131, 273
Hammer, N. J., Janka, H.-T., & Müller, E. 2010, ApJ, 714, 1371
Hanke, F., Marek, A., Müller, B., & Janka, H.-T. 2012, ApJ, 755, 138
Hanke, F., Müller, B., Wongwathanarat, A., Marek, A., & Janka, H.-T. 2013, ApJ, 770, 66
Hobbs, G., Lorimer, D. R., Lyne, A. G., & Kramer, M. 2005, MNRAS, 360, 974
Janka, H.-T. 2001, A&A, 368, 527
Joggerst, C. C., Almgren, A., & Woosley, S. E. 2010, ApJ, 723, 353
Lai, D., & Goldreich, P. 2000, ApJ, 535, 402
Langer, N. 2012, ARA&A, 50, 107
Lee, D., Tzeferacos, P., Couch, S. M., & et al. 2013, in preparation
Meakin, C. A., & Arnett, D. 2007, ApJ, 667, 448
Müller, B., Janka, H.-T., & Marek, A. 2012, ApJ, 756, 84
Murphy, J. W., & Burrows, A. 2008, ApJ, 688, 1159
O'Connor, E., & Ott, C. D. 2010, CQGra, 27, 114103
Ott, C. D., Burrows, A., Dessart, L., & Livne, E. 2008, ApJ, 685, 1069
Ott, C. D., Abdikamalov, E., O'Connor, E., et al. 2012, Phys. Rev. D, 86, 24026
Ott, C. D., Abdikamalov, E., Mösta, P., et al. 2013, ApJ, 768, 115
Quataert, E., & Shiode, J. 2012, MNRAS, 423, L92
Scheck, L., Janka, H.-T., Foglizzo, T., & Kifonidis, K. 2008, A&A, 477, 931
Smith, N., & Arnett, D. 2013, submitted to ApJ, arXiv:1307.5035
Takiwaki, T., Kotake, K., & Suwa, Y. 2013, Submitted to ApJ, arXiv:1308.5755
Thompson, C. 2000, ApJ, 534, 915
Thompson, T. A., Quataert, E., & Burrows, A. 2005, ApJ, 620, 861
Vink, J. 2012, A&A Rev., 20, 49
Wang, L., & Wheeler, J. C. 2008, ARA&A, 46, 433
Woosley, S., & Heger, A. 2007, Phys. Rep., 442, 269